

# Using Active Learning to Improve Quasar Identification for the DESI Spectra Processing Pipeline

Dylan Green<sup>1</sup>, David Kirkby<sup>1</sup>, J. Aguilar<sup>2</sup>, S. Ahlen<sup>3</sup>,  
D. M. Alexander<sup>4,5</sup>, E. Armengaud<sup>6</sup>, S. Bailey<sup>2</sup>, A. Bault<sup>2</sup>,  
D. Bianchi<sup>7,8</sup>, A. Brodzeller<sup>2</sup>, D. Brooks<sup>9</sup>, T. Claybaugh<sup>2</sup>,  
R. de Belsunce<sup>2</sup>, A. de la Macorra<sup>10</sup>, P. Doel<sup>9</sup>,  
V. A. Fawcett<sup>11</sup>, S. Ferraro<sup>2,12</sup>, A. Font-Ribera<sup>13</sup>,  
J. E. Forero-Romero<sup>14,15</sup>, E. Gaztañaga<sup>16,17,18</sup>, S. Gontcho A  
Gontcho<sup>2</sup>, G. Gutierrez<sup>19</sup>, M. Ishak<sup>20</sup>, S. Juneau<sup>21</sup>,  
R. Kehoe<sup>22</sup>, T. Kisner<sup>2</sup>, A. Kremin<sup>2</sup>, A. Lambert<sup>2</sup>,  
M. Landriau<sup>2</sup>, L. Le Guillou<sup>23</sup>, M. E. Levi<sup>2</sup>, M. Manera<sup>24,13</sup>,  
A. Meisner<sup>21</sup>, R. Miquel<sup>25,13</sup>, J. Moustakas<sup>26</sup>, A. D. Myers<sup>27</sup>,  
N. Palanque-Delabrouille<sup>6,2</sup>, F. Prada<sup>28</sup>, I. Pérez-Ràfols<sup>29</sup>,  
G. Rossi<sup>30</sup>, E. Sanchez<sup>31</sup>, C. Saulder<sup>32</sup>, D. Schlegel<sup>2</sup>,  
M. Schubnell<sup>33,34</sup>, H. Seo<sup>35</sup>, F. Sinigaglia<sup>36,37</sup>, D. Sprayberry<sup>21</sup>,  
T. Tan<sup>6</sup>, G. Tarlé<sup>34</sup>, B. A. Weaver<sup>21</sup>, S. Youles<sup>17</sup>, J. Yu<sup>38</sup>,  
R. Zhou<sup>2</sup>, H. Zou<sup>39</sup>

<sup>1</sup>Department of Physics and Astronomy, University of California, Irvine, 92697, USA

<sup>2</sup>Lawrence Berkeley National Laboratory, 1 Cyclotron Road, Berkeley, CA 94720, USA

<sup>3</sup>Department of Physics, Boston University, 590 Commonwealth Avenue, Boston, MA 02215 USA

<sup>4</sup>Centre for Extragalactic Astronomy, Department of Physics, Durham University, South Road, Durham, DH1 3LE, UK

<sup>5</sup>Institute for Computational Cosmology, Department of Physics, Durham University, South Road, Durham DH1 3LE, UK

<sup>6</sup>IRFU, CEA, Université Paris-Saclay, F-91191 Gif-sur-Yvette, France

<sup>7</sup>Dipartimento di Fisica “Aldo Pontremoli”, Università degli Studi di Milano, Via Celoria 16, I-20133 Milano, Italy

<sup>8</sup>INAF-Osservatorio Astronomico di Brera, Via Brera 28, 20122 Milano, Italy

<sup>9</sup>Department of Physics & Astronomy, University College London, Gower Street, London, WC1E 6BT, UK

<sup>10</sup>Instituto de Física, Universidad Nacional Autónoma de México, Circuito de la Investigación Científica, Ciudad Universitaria, Cd. de México C. P. 04510, México

- <sup>11</sup>School of Mathematics, Statistics and Physics, Newcastle University, Newcastle upon Tyne, NE1 7RU, UK
- <sup>12</sup>University of California, Berkeley, 110 Sproul Hall #5800 Berkeley, CA 94720, USA
- <sup>13</sup>Institut de Física d'Altes Energies (IFAE), The Barcelona Institute of Science and Technology, Edifici Cn, Campus UAB, 08193, Bellaterra (Barcelona), Spain
- <sup>14</sup>Departamento de Física, Universidad de los Andes, Cra. 1 No. 18A-10, Edificio Ip, CP 111711, Bogotá, Colombia
- <sup>15</sup>Observatorio Astronómico, Universidad de los Andes, Cra. 1 No. 18A-10, Edificio H, CP 111711 Bogotá, Colombia
- <sup>16</sup>Institut d'Estudis Espacials de Catalunya (IEEC), c/ Esteve Terradas 1, Edifici RDIT, Campus PMT-UPC, 08860 Castelldefels, Spain
- <sup>17</sup>Institute of Cosmology and Gravitation, University of Portsmouth, Dennis Sciamia Building, Portsmouth, PO1 3FX, UK
- <sup>18</sup>Institute of Space Sciences, ICE-CSIC, Campus UAB, Carrer de Can Magrans s/n, 08913 Bellaterra, Barcelona, Spain
- <sup>19</sup>Fermi National Accelerator Laboratory, PO Box 500, Batavia, IL 60510, USA
- <sup>20</sup>Department of Physics, The University of Texas at Dallas, 800 W. Campbell Rd., Richardson, TX 75080, USA
- <sup>21</sup>NSF NOIRLab, 950 N. Cherry Ave., Tucson, AZ 85719, USA
- <sup>22</sup>Department of Physics, Southern Methodist University, 3215 Daniel Avenue, Dallas, TX 75275, USA
- <sup>23</sup>Sorbonne Université, CNRS/IN2P3, Laboratoire de Physique Nucléaire et de Hautes Energies (LPNHE), FR-75005 Paris, France
- <sup>24</sup>Departament de Física, Serra Húnter, Universitat Autònoma de Barcelona, 08193 Bellaterra (Barcelona), Spain
- <sup>25</sup>Institució Catalana de Recerca i Estudis Avançats, Passeig de Lluís Companys, 23, 08010 Barcelona, Spain
- <sup>26</sup>Department of Physics and Astronomy, Siena College, 515 Loudon Road, Loudonville, NY 12211, USA
- <sup>27</sup>Department of Physics & Astronomy, University of Wyoming, 1000 E. University, Dept. 3905, Laramie, WY 82071, USA
- <sup>28</sup>Instituto de Astrofísica de Andalucía (CSIC), Glorieta de la Astronomía, s/n, E-18008 Granada, Spain
- <sup>29</sup>Departament de Física, EEBE, Universitat Politècnica de Catalunya, c/Eduard Maristany 10, 08930 Barcelona, Spain
- <sup>30</sup>Department of Physics and Astronomy, Sejong University, 209 Neungdong-ro, Gwangjin-gu, Seoul 05006, Republic of Korea
- <sup>31</sup>CIEMAT, Avenida Complutense 40, E-28040 Madrid, Spain
- <sup>32</sup>Max Planck Institute for Extraterrestrial Physics, Gießenbachstraße 1, 85748 Garching, Germany
- <sup>33</sup>Department of Physics, University of Michigan, 450 Church Street, Ann Arbor, MI 48109, USA
- <sup>34</sup>University of Michigan, 500 S. State Street, Ann Arbor, MI 48109, USA
- <sup>35</sup>Department of Physics & Astronomy, Ohio University, 139 University Terrace, Athens, OH 45701, USA

<sup>36</sup>Departamento de Astrofísica, Universidad de La Laguna (ULL), E-38206, La Laguna, Tenerife, Spain

<sup>37</sup>Instituto de Astrofísica de Canarias, C/ Vía Láctea, s/n, E-38205 La Laguna, Tenerife, Spain

<sup>38</sup>Institute of Physics, Laboratory of Astrophysics, École Polytechnique Fédérale de Lausanne (EPFL), Observatoire de Sauverny, Chemin Pegasi 51, CH-1290 Versoix, Switzerland

<sup>39</sup>National Astronomical Observatories, Chinese Academy of Sciences, A20 Datun Road, Chaoyang District, Beijing, 100101, P. R. China

E-mail: [dylanag@uci.edu](mailto:dylanag@uci.edu)

**Abstract.** The Dark Energy Spectroscopic Instrument (DESI) survey uses an automatic spectral classification pipeline to classify spectra. QuasarNET is a convolutional neural network used as part of this pipeline originally trained using data from the Baryon Oscillation Spectroscopic Survey (BOSS). In this paper we implement an active learning algorithm to optimally select spectra to use for training a new version of the QuasarNET weights file using only DESI data, specifically to improve classification accuracy. This active learning algorithm includes a novel outlier rejection step using a Self-Organizing Map to ensure we label spectra representative of the larger quasar sample observed in DESI. We perform two iterations of the active learning pipeline, assembling a final dataset of 5600 labeled spectra, a small subset of the approx 1.3 million quasar targets in DESI’s Data Release 1. When splitting the spectra into training and validation subsets we meet or exceed the previously trained weights file in completeness and purity calculated on the validation dataset with less than one tenth of the amount of training data. The new weights also more consistently classify objects in the same way when used on unlabeled data compared to the old weights file. In the process of improving QuasarNET’s classification accuracy we discovered a systemic error in QuasarNET’s redshift estimation and used our findings to improve our understanding of QuasarNET’s redshifts.

---

## Contents

<b>1</b>	<b>Introduction</b>	<b>1</b>
<b>2</b>	<b>New QuasarNET Structure</b>	<b>3</b>
<b>3</b>	<b>Active Learning and Dataset Selection</b>	<b>5</b>
<b>4</b>	<b>Results</b>	<b>7</b>
4.1	Results on Labeled Data	9
4.2	Results on Unlabeled Data	11
4.2.1	Classification and Consistency Results	12
4.2.2	Redshift Results and Identifying an Issue with QuasarNET	14
<b>5</b>	<b>Conclusions</b>	<b>16</b>

---

## 1 Introduction

The Dark Energy Spectroscopic Instrument (DESI) is an ongoing spectroscopic survey that aims to observe over 40 million objects over the course of five years, with the goal of mapping the expansion history of the universe [1, 2]. DESI is mounted on the Mayall 4-meter telescope at Kitt Peak National Observatory and will map approximately a third of the night sky over the course of the survey [3, 4]. DESI takes an exposure of up to 5000 spectra at a time, a significant increase in data collection over previous spectroscopic surveys [5–7]. To date [8] approximately one million spectra have been released publicly as the DESI Early Data Release (EDR) [9, 10], with Data Release 1 (DR1) forthcoming.

The first data release of the DESI instrument [11] includes key science papers presenting the cosmological results of the first year of data collection. These results span a variety of different cosmology probes, and include two point clustering [8], Baryon Acoustic Oscillation (BAO) and full shape results from both quasars and galaxies [12, 13] and BAO results from the Lyman-alpha forest [14]. DESI also reports cosmological constraints from the BAO results [15] and the full shape analysis [16].

As part of its data collection, DESI employs a state-of-the-art data processing pipeline that automatically classifies each spectrum [17, 18], Redrock [19], which uses Principal Component Analysis templates fit at different trial redshifts. While overall very accurate, Redrock is slightly less accurate when identifying quasars compared to other galaxy sub types. To this end, QuasarNET was added to the DESI classification pipeline to recover quasars missed by Redrock [20]. QuasarNET is a convolutional neural network that can automatically identify quasars and provide an estimated redshift based on observed emission line positions [21, 22]. We refer readers to [20] for a more detailed description of how QuasarNET contributes to DESI’s classification pipeline.

QuasarNET originally consisted of four convolution layers followed by a fully connected layer. This fully connected layer was then connected to a series of fully connected layers of 26 outputs each. The number of fully connected layers is determined by how many quasar emission lines QuasarNET is trained on. Intrinsically, QuasarNET is a *line-finder* network, and its primary output from each output layer is an estimated position for the emission line

associated with that fully connected layer. The first 13 outputs of each line-finder unit is a confidence value that the given emission line is present within that portion or “box” subset of the wavelength range, a coarse-grained estimate of the line position. The second 13 outputs are fine-grained estimates of line positions within each of the 13 boxes and are floating point values between -0.1 and 1.1, where 0 corresponds with the lower edge of the box and 1 corresponds with the upper edge. Classification of spectra using these outputs is done by selecting a confidence threshold and a number threshold and assigning a quasar classification to any spectra where more lines than the number threshold have confidence values above the confidence threshold. This means that classification only uses the first 13 outputs of each line-finder unit. QuasarNET also provides a redshift estimate for each spectrum, producing an independent redshift estimate for each emission line detected in the spectrum. Redshift estimation is done by using the combined estimated line position (coarse + fine) to estimate a central wavelength of an emission line, which is then converted to a redshift using the rest-frame wavelength associated with that line-finder unit. [21] provides a more in-depth explanation of how QuasarNET works.

Within the DESI pipeline, QuasarNET is run on *all* spectra, but its results are only used when redrock classifies a spectrum as a galaxy and QuasarNET classifies the same spectrum as a quasar with a confidence threshold of 0.95 and a number threshold of 1. When this occurs, QuasarNET will trigger a rerun of Redrock using only the quasar templates and a uniform flat prior on redshift centered at the QuasarNET redshift with a width of  $\Delta z = 0.1$ .

Since QuasarNET is a deep neural network, its performance heavily depends on the weights file. The weights file used in DESI EDR and DR1 analyses was originally trained on data from eBOSS with truth labels provided by visual inspection (VI) in DR12 [23]. The eBOSS dataset, however, is a suboptimal training sample for the DESI spectral sample set for a few core reasons:

- BOSS and later eBOSS used a log-linear wavelength grid for spectral extraction, and correspondingly QuasarNET uses a log-linear grid based on the eBOSS grid. The eBOSS grid used a constant  $\Delta \log \lambda = 10^{-3}$  spacing while the QuasarNET grid was designed with  $\Delta \log \lambda = 10^{-2}$ . DESI, on the other hand, uses a linear wavelength grid, with a constant linear spacing  $\Delta \lambda = 0.8$ .
- The flux calibration, and by extension the signal to noise ratio, between eBOSS and DESI differ over the course of the wavelength region, which might affect the success rate of QuasarNET on DESI spectra.
- The BOSS spectrograph had only a single dichroic [24], which means that each spectrum was captured in two parts and then coadded into a single wavelength region. DESI, in comparison, has two dichroics and therefore three different wavelength regions. Due to this design, DESI uses a different sensor in the lowest wavelength region than in the upper two, both of which differ from the BOSS sensors. The noise response of these three sensors differ, but QuasarNET does not include any error or inverse variance information. This means that while correct error handling can account for these differences, QuasarNET might not.

In this paper we modify QuasarNET to better accommodate DESI data, improving its capabilities and performance. These modifications come in two forms: adjustments to the network structure, and careful selection of training data, with our novel contribution being the use of active learning to self select a training sample comprised of only DESI data. Due

to the large amount of candidate data we additionally include a novel outlier rejection step to improve the efficiency of the dataset selection.

After outlining our modifications to QuasarNET, we outline the active learning methodology and its application to improving QuasarNET’s classification accuracy and purity when coupled with the aforementioned network changes. Ideally we would like a comparable amount of DESI data to train a new weights file to improve QuasarNET’s handling of DESI data. The sheer quantity of spectra observed by DESI, however, makes visual inspection of DESI data on a similar scale unfeasible, so by construction any training dataset comprised of DESI data will have significantly fewer spectra than that comprised of eBOSS data. To combat this reduced amount of training data we apply the active learning methodology to select an optimal set of data to be labeled that will provide the largest improvement in the network when trained. We couple this with a novel outlier rejection step designed to further ensure that the spectra we select to label provide adequate coverage of the possible data space. By doing this we are able to significantly improve QuasarNET’s performance on DESI data even when using a much smaller training dataset of approximately 6k spectra, only 10% of the previous training sample.

Our quasar dataset significantly improves the completeness of our classifications without sacrificing purity, which we demonstrate by splitting our selected sample into training and hold out validation sets. We then demonstrate the new QuasarNET’s performance on unlabeled data by comparing the classification and redshift estimates of repeated exposures of the same objects. In this test we further demonstrate the power of our new dataset with improved repeat classification accuracy, with QuasarNET more consistently classifying objects the same way in multiple exposures.

Our work in this paper was focused only on classification accuracy, but QuasarNET also provides redshift estimates that are used in the DESI pipeline. When studying the repeat exposure tests we uncovered a significant “oscillation” problem with QuasarNET redshift estimates. We will outline the issue and its causes, which are not a result of the active learning methodology presented in this paper. At the end of the paper will very briefly describe a solution to the problem that was driven by the understanding gained in this work.

## 2 New QuasarNET Structure

Before selection of a training set we adjust the QuasarNET input to better accommodate the DESI instrument’s output, since QuasarNET was originally designed for eBOSS data. We do this by directly modifying the QuasarNET architecture to better handle the DESI data and its differences from the previous eBOSS data by adding padding, which increase the amount of convolutions we can include, and by adding dropout, which helps improves the network’s generalizability especially with small training samples.

Figure 1 shows the QuasarNET model structure prior to this work, originally defined in [21], along the top row. The network was constructed of four consecutive convolution layers, each with the same parameters. The layers have no padding, a stride of two, a convolution kernel width of 10, and a filter size of 100. The four convolution layers are followed by a fully connected layer of width 100, which then feeds into 14 parallel individual fully connected layers called line finders, 2 for each line, with 13 outputs each. The line finders each produce an independent output estimate of that emission line’s position in the input spectrum, with one block of 13 producing a coarse estimate and the second a fine grained estimate on top of the coarse one. These layer outputs are then used for classification and redshift estimation,

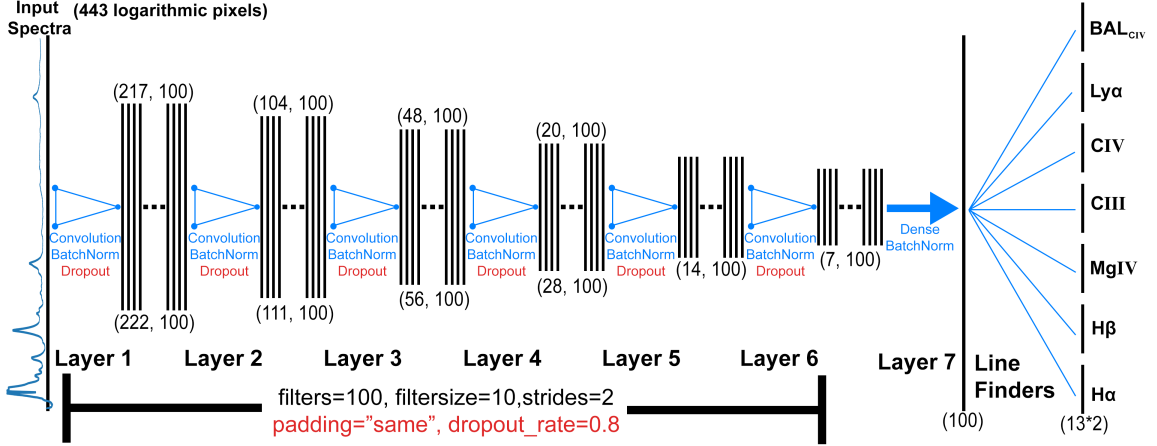


**Figure 1.** QuasarNET architecture, both before and after this work. Along the top are the sizes of the outputs of each layer prior to this work, and below are the numbers after this work. In red along the bottom and at each layer step denote hyperparameters that have been changed by this work. The addition of padding in each convolutional layer allows the inclusion of two additional convolutions, the former structure connected the output of layer 4 directly to the fully connected layer. As before, each line finder is constructed of two fully connected layers, each with 13 outputs, for a total of 26 outputs for each line finder. See text for a more details on the specific changes from prior work.

with an independent result returned for each emission line. QuasarNET only estimates a redshift if it detects emission lines in the input spectrum, and although it computes the redshift for all predicted emission lines, in practice only the redshift estimate from the most confident line is used.

To improve QuasarNET’s performance on DESI data we make two significant changes to the network structure motivated by the limited amount of DESI training data and differences in data structure and quality. This new structure is also included in Figure 1, along the bottom row. Hyperparameters for each layer are printed below each layer, with changes highlighted in red across the plot. We summarize these changes below.

Firstly, we add dropout layers to each convolution block after the batch normalization step. Dropout layers randomly select a subset of input units and prevent them from being trained in a given training epoch, repeating this procedure anew at each epoch. Dropout layers have been shown to help compensate for a reduced amount of input training data by only training a subset of weights at each training step, improving the generalization of the network. Additionally, they have been shown to prevent over fitting, a minor concern when examining loss curves for the previous eBOSS dataset[25, 26]. Dropout layers have a single hyper parameter corresponding to the frequency at which units are held out from training, which we set to 0.8, which means that 80% of the trainable parameters will be zeroed out and not trained at each epoch. [26] recommends that a value of 0.5 tends to be optimal for a wide variety of tasks, but in empirical tests we found 0.8 to give the best performance with our specific architecture.

Secondly we add edge padding to the dataset prior to each convolution step. We pad each matrix with zeroes using the Tensorflow option “same”, which pads the matrix with enough values such that a convolution with a stride of one will output a matrix with the same width as the input matrix. For our network we pad with zeroes, although in general other values could be used. We do not change the stride value of the network, leaving it at two.

Due to the new padding each layer will now decrease in width by a factor of two after each convolution, rather than losing half plus the width of the convolution filter. This can be seen by comparing the widths of each layer in Figure 1 between the old structure (top) and new structure (bottom). This subtle but important difference allows us to add an additional two convolution layers before the fully connected layer.

### 3 Active Learning and Dataset Selection

During the first few months of the DESI survey a selection of deep tiles were visually inspected to quantify the performance of the automatic DESI classification pipeline [27, 28]. These efforts visually inspected approximately 16000 galaxy targets of various subtypes and approximately 8500 quasar targets. We initially attempted to train QuasarNET using a subset of these spectra as a training dataset, keeping all the quasar specific tiles and a small subset of galaxies from the galaxy tiles. The small size of this dataset limited the performance of QuasarNET.

To further improve performance we decided to label additional DESI spectra to supplement those already labeled in prior VI campaigns. Since the amount of human effort to label and classify spectra is non-trivial, we want to minimize the amount of new spectra necessary to improve QuasarNET’s performance while maximizing its associated impact. This is especially true even though we use only the first few months of DESI data as a potential training set. This data will be released as part of DESI’s DR1, and represents the first few months of DESI main survey observations, over 3.6 million spectra, processed in the “Guadalupe” data reduction. In order to select which of these spectra to label and include in training we use the active learning algorithm. For an in depth and comprehensive exploration of active learning, its implementation, and its mathematics, we recommend [29].

Briefly, active learning uses an algorithm’s classification uncertainty to quantify which unlabeled data is most confusing to the network. This confusing data is then passed to a human expert who labels them for inclusion in a new training run. By continuously training on confusing data we can maximize the performance of the algorithm with the smallest amount of data, as we are continuously filling the network’s (or other algorithm’s) gaps in knowledge. When used with a classification algorithm active learning will tend to pick data points that lie along decision boundaries, i.e. those that have the highest uncertainty and thus the largest possibility of classification confusion.

Active learning has been used successfully in astronomical research to identify anomalous data to specifically train networks to automatically identify *interesting* anomalous data [30] and to outsource labeling of galaxy images to citizen scientists to speed classification and improve automatic pipelines [31]. These prior applications of active learning in astrophysics have focused on image classification networks, which take in a 2-D image and produce a single classification value. QuasarNET, however, does not directly do classification, nor does it use 2-D images, instead focusing on identifying emission line positions from 1-D spectra with classification and redshift estimation as post-processing on the raw network outputs. We believe that for these reasons our application of active learning is novel in scope.

Since QuasarNET is a line finder, only outputting estimated line positions for each of the lines in the input set, QuasarNET does not output an uncertainty value as part of its results. Classification is done by categorizing objects as a quasar if they have at least one of the requisite emission lines with a large enough confidence. In order to generate uncertainty values for use with active learning we use bootstrapping to create 200 separate weights files using

the same input dataset. Each of the weights files are trained using the same parameters, the only difference is the data used in training each weights file, which is bootstrapped such that each network has the same amount of training data, but different (and possibly duplicated) subsets of the possible data pool.

Once we have an ensemble of networks we use the networks to classify each spectrum as either a quasar or not, using a confidence threshold of 0.95. This is the same confidence threshold used in DESI. When implementing active learning with only two category classification the algorithm will pick spectra that lie along the 50% confusion boundary. It is more interesting and informative to instead use three or more categories, where spectra that have high confusion between two categories have the possibility of being strongly identified as *not* belonging to the third. To emulate this we split the quasar classification into two separate categories: HIGH-Z and LOW-Z. We use an estimated value of  $z = 2.1$  as the division between these categories, as this is the approximate redshift that the Lyman- $\alpha$  line will become visible enough in the DESI spectrograph for QuasarNET to reliably detect. An added benefit of this split is that we can incorporate some estimated redshift information into the active learning algorithm. The division boundary between NOT QSO and the two QSO categories will be dominated by whether or not the network has detected any emission lines, while the boundary between the LOW-Z and HIGH-Z QSO categories is dominated by redshift estimation. Once we have the output of the 200 networks we convert them to confidence values such that each potential unlabeled spectrum has three confidence values defined by

$$C_{\text{CLASS}} = \frac{N_{\text{CLASS}}}{N_{\text{ENSEMBLE}}}, \quad (3.1)$$

where  $N_{\text{CLASS}}$  is the number of networks that classified the spectrum with the given classification and  $N_{\text{ENSEMBLE}} = 200$  is the total number of networks in the ensemble. We use these confidence values to calculate the entropy of each spectrum,

$$H = \sum_{\text{CLASSES}} -C_i \log_2 C_i, \quad (3.2)$$

which we use to determine which spectra we will visually inspect, using entropy as a confusion metric for data selection. The choice of  $\log_2$  is motivated by the choice to use units of bits, which are more easily interpretable. Spectra that have higher entropy have more confusion, lying near or on the boundaries between two or all three of the target classes.

Traditionally, active learning considers all possible unlabeled data (in this case spectra) as potential training data in its initial pass. Since labeling spectra is a time intensive task, and there is a non-trivial amount of anomalous or otherwise unusual spectra, we have added an additional and novel outlier rejection step to the active learning process. By doing so we ensure that spectra chosen to be inspected are useful for training the network and *also* spectra that are expected to be representative of the larger DESI spectral sample, as opposed to outlier or unusual spectra. This outlier rejection step uses a self-organizing map (SOM) to identify similar spectra to each other in a two dimensional reduced space.

A SOM is an unsupervised machine learning algorithm that divides a requested latent space into a set number of cells. At each iteration of the algorithm data points that share characteristics are assigned to the same or nearby cells, such that the final product is a set of weights that classifies input data into an assigned cell. For a more detailed theoretical review of how SOMs work, we refer the reader to [32]. SOMs have been used variously in astrophysics, with some examples including directly classifying objects and estimating their

redshifts [33] and performing photometric redshift calibration [34]. In our work we do not use the SOM directly for redshift estimation or classification, using it only as part of our active learning pipeline to reject anomalous spectra. We use the package SOMVIZ [35] to train our SOM.

When training our SOM, we use the rebinned spectra exactly as they are input to the QuasarNET algorithm, to ensure that it learns spectral characteristics from the same data as our network. The SOM trained and used in our procedure is plotted in Figure 2. In each panel the color of each cell correlates with how many spectra are assigned to that cell. We have split the SOM into four panels, with each panel representing spectra in one of the four possible input truth table labels, to demonstrate how the SOM has associated similar spectra into localized clumps within the requested two-dimensional space.

When we select a sample of spectra to visually inspect and label, we reject any selections whose cell in the SOM has a total number of spectra below a chosen threshold value. This has the effect of ensuring that the final selected spectra to label are localized within the SOM to locations that have a high density of similar spectra. For this work, we selected a threshold value equal to the 15th percentile of spectra counts in all cells.

The output of a single iteration of the entire active learning algorithm is represented in Figure 3. We start with a potential dataset of 3.6 million spectra and apply the SOM based outlier rejection step to eliminate 15.5 thousand spectra from the pool of potential training data. We then apply a cut, removing repeat exposures of the same object to ensure that we have unique objects to visually inspect rather than multiple exposures of the same objects. This reduces the pool of spectra to just below 3 million unique objects. In Figure 3 we plot a histogram of the entropy values, defined in Eq. 3.2, of the remaining spectra.

A red line indicates the cutoff we selected, above which there are 1000 spectra that we request to be visually inspected and labeled. We select 1000 spectra to balance the impact the new data has on the network against the speed at which we can visually inspect spectra. The plot shows two notable features: first, there is a sharp peak at zero, representing a large set of spectra for which there is high degree of confidence and agreement in the ensemble classification. Second, there is a sharp dropoff near 1 corresponding to the point at which a spectrum lies at the 50% confusion boundary between two classes, with no classifications in the third. Above this point in the histogram are spectra that show significant confusion between all three classes, rather than being either confused between only two classes or highly confident in one and weakly confident in the others.

## 4 Results

We ran the active learning pipeline twice, selecting 1000 spectra at each step to visually inspect and label. At the initial step we use 3761 DESI spectra from quasar dense tiles (“Deep-field VI” from Table 1 of [27]) plus an additional 839 DESI spectra from non-quasar dense tiles (a subset of all spectra in Table 1 of [28]) which we include to ensure that the dataset is not overly quasar dense. These 4600 DESI spectra were visually inspected and the results validated in [27, 28]. We then augment this dataset with an additional 15000 spectra from the previous eBOSS training dataset. We are motivated to supplement the DESI-only dataset for the first pass because the DESI only dataset does not fully cover the possible quasar space. For the second active learning step we use only the originally labeled DESI spectra plus the additional 1000 labeled spectra from the first active learning step to train the networks, excluding the supplemental eBOSS data, as we now consider it representative of

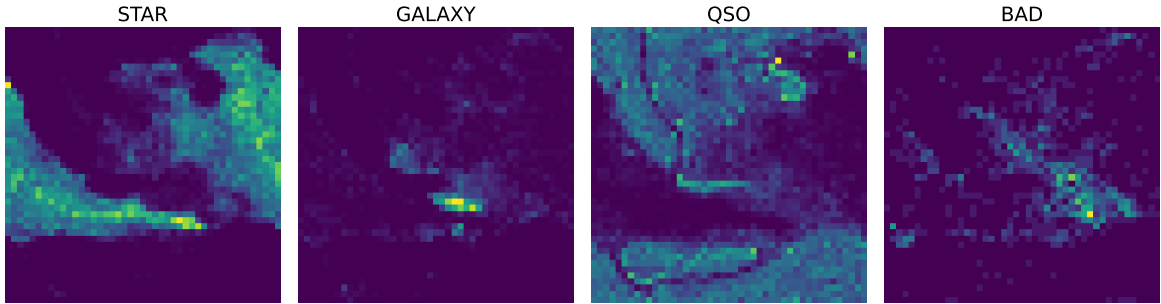


**Figure 2.** Two-dimensional representation of the self-organizing map (SOM) used for outlier rejection during active learning. The SOM is square, with 45 cells on each side. In each panel the color in each cell correlates to how many spectra are assigned to that cell by the SOM. We have split the SOM into four panels, with each panel representing one of the possible visual inspection truth labels. By doing this it becomes evident that the SOM has localized similar spectra into self contained segments of the SOM. Quasars have the largest diversity in our training data, so take up a larger portion of the SOM.

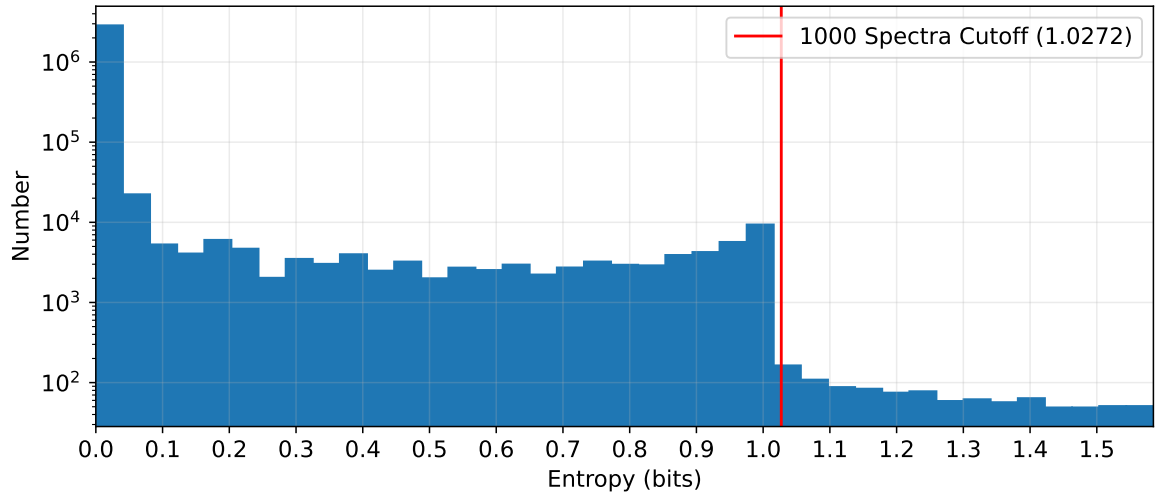


**Figure 3.** A distribution of entropy values in the unlabeled dataset calculated using the prior weights file. The red line denotes the cutoff above which the 1000 spectra we opted to VI lie, with the value at which this occurs denoted on the plot. The sharp drop off at around 1 is likely due to the construction of our three classification classes. Since two of them represent quasar classifications, LOZ and HIZ QSOs, and one does not, it is not equally likely that spectra will fall into all three classifications based on spectral type alone.

the DESI quasar observation space, and believe that the active learning algorithm will select spectra to fill any deficiencies.

For the visual inspection steps in the active learning pipeline we require that two separate experts inspect each spectra, assigning an estimated redshift and spectral classification as well as a “quality” rating (on a scale of 0-4, with 4 the most confident) that quantifies how confident the inspector is in their labels. Each spectra is then inspected by a “merger” who resolves discrepancies in the two results and assigns a final quality rating. QuasarNET only uses spectra whose final quality is above 2.5. A more detailed description of this procedure is available in [27] and [28].

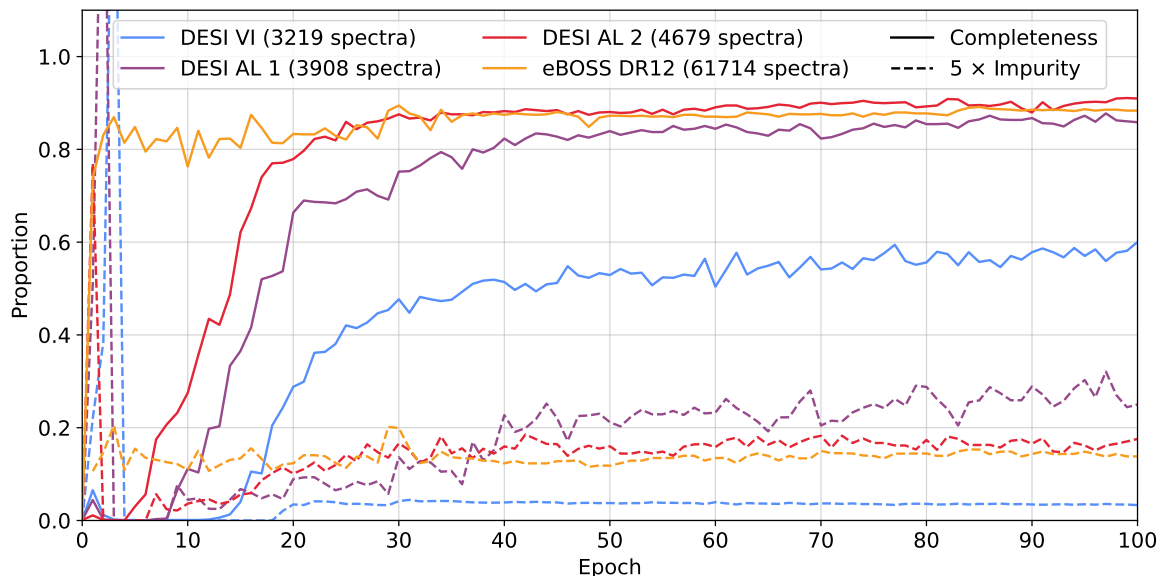


**Figure 4.** Purity and completeness on the validation dataset per epoch of training. Purity is the proportion of classified quasars that are true quasars and completeness is the proportion of true quasars that are correctly classified as quasars. Completeness is plotted in solid curves while in dotted we plot  $5 \times$  impurity for visual clarity. In yellow is a training run using the previous eBOSS based dataset for training; while red, blue and magenta are DESI only datasets. Blue is training on just spectra from DESI Visual Inspection, magenta is after including the results of the first active learning iteration, while red is after the second active learning iteration. When including the additional data determined through active learning we are able to achieve comparable or better performance than the eBOSS trained dataset with less than one tenth of the amount of data.

We present the results of this two-step procedure in two subsections, in the first we report results using the full truth dataset which we split into training and validation subsets. In the second we test the final DESI-specific weights file, trained on the entirety of the truth table rather than a subset. The weights testing used the internal data release “Guadalupe”, which will be included in DESI’s Data Release 1 (DR1), where we have no truth data but for which we do have a set of metrics that quantify this weights file’s improvement over the previous version. These metrics include consistency in classification and redshift uncertainty. In the second section we will also outline the new understanding of QuasarNET’s redshift estimation problems, which became apparent when using this newly trained weights file.

#### 4.1 Results on Labeled Data

In this section we train a weights file using a subset of the full truth table, which includes the original set of visually inspected quasar tiles (3761 spectra), the additional subset of other galaxy dense visually inspected tiles (839 spectra), and the results of two active learning runs (2100 spectra). The total number of spectra in the truth table is 6700, although after training we discovered 2 spectra whose data processing was corrupted or otherwise nonphysical that were affecting training and removed them for a grand total of 6698 labeled spectra. We split this dataset into two subsets such that 70% of the data is used for training and the other 30% is used for testing and validation. In order to validate that the inclusion of the active learning spectra has improved the network’s performance notably we compare this training

to two other training schemes. In one run we use the subset of the training dataset that excludes those spectra added after the second active learning step (keeping those spectra labeled in the first active learning run) and in the other run we use the same eBOSS dataset for training that was used to train the prior DESI weights file. All three runs use the same validation dataset. The results of these three runs are shown in Figure 4, with the eBOSS run in green, the results after the first visual inspection run in red and the results after both visual inspection runs in blue. For this plot, we use a confidence threshold of 0.95, thus declaring that QuasarNET identifies a quasar if it has at least one line with a confidence of more than 0.95.

Completeness, defined as

$$C = \frac{N_{\text{QSO,PRED}}}{N_{\text{QSO,TRUE}}}, \quad (4.1)$$

is plotted in Figure 4 as a solid line per epoch of training and is the proportion of true quasars that are correctly identified as such by QuasarNET with 1 meaning that every quasar is correctly identified by QuasarNET. Purity is the proportion of spectra that are classified as quasars by QuasarNET that are true quasars, with 1 representing that all predicted quasars are truly quasars. For visual clarity we plot *impurity* (in dashed) rather than purity, which we define as

$$I = 1 - P = 1 - \frac{N_{\text{QSO,TRUE \& QSO,PRED}}}{N_{\text{QSO,PRED}}}. \quad (4.2)$$

As validated in the plot, the second visual inspection run gave a significant improvement in completeness at approximately the same (although marginally better) purity at each epoch, reaching a high maximum completeness faster than after the first visual inspection run. Also notable is the equivalent or higher completeness and purity per iteration at its maximum compared to the prior eBOSS training, validating that a DESI only dataset improves over an eBOSS one when used with DESI validation data.

It is possible that a larger dataset could explain some or all of the improvement at each active learning step. In order to validate that our improvement is more significant than dataset size alone, we bootstrap each of the two earlier runs, the pre-active learning and the post first iteration active learning, to have the same amount of data as the final assembled dataset. We perform 10 unique bootstraps of each dataset, for 20 total unique datasets of the same size as the final dataset, and then train for 100 epochs with the same parameters as the previous test. The results of this test are shown in Figure 5. For clarity we plot only the completeness, although purity follows a similar trend. The solid lines represent the same completeness curves as plotted in Figure 4. In dashed blue and dashed magenta are the 10 bootstrap runs for the pre-active learning and post first iteration datasets, respectively. Although the increased amount of data does have some effect on the training it does not significantly alter the final best completeness values. In none of the bootstrap datasets does the training reach the level of completeness that our final dataset provides. This further validates that our active learning pipeline has specifically chosen spectra that give significant improvements to the training cycle.

For our active learning pipeline we used a confidence threshold of 0.95, meaning that any spectrum with at least one line with a confidence more than 0.95 was considered a quasar. This motivated the choice used in the loss curves in Figure 4 and Figure 5, where the purity and completeness per epoch were calculated using this same confidence threshold. It is also informative to explore how the choice of confidence threshold changes the final results of the network. In Figure 6 we plot the purity and completeness against each other, with each point

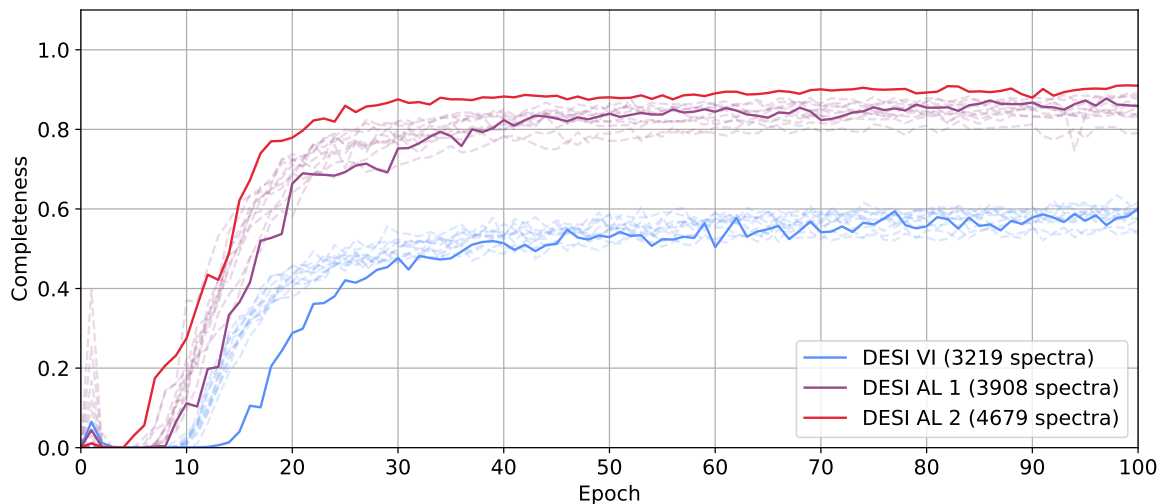


**Figure 5.** Completeness calculated on the validation dataset per epoch of training, with bootstraps. In solid we plot the completeness per epoch of training, the same data as in Figure 4. In dashed are bootstrapped realizations of the two smaller datasets. We bootstrap the smaller datasets to have the same amount of data as the largest (after the 2nd active learning run) in order to validate that the improvements when adding the active learning data at each step are, at least in part, due to the specific data chosen rather than the increase in dataset size. For both smaller datasets the bootstrapped datasets do not reach the same level of completeness, nor do they reach their maximum as quickly, as the final dataset. For clarity we have plotted only completeness, but purity follows the same trend.

computed using a different confidence threshold between zero and one. This curve shows the trade off between improved completeness and lower purity at lower thresholds and the opposite at higher thresholds. Large dots indicate the values of both quantities at our test threshold of 0.95. In the plot we see that at our threshold of 0.95 we have succeeded in improving the completeness of the final weights file, with almost identical purity. This effect does not hold true at all confidence thresholds. At lower thresholds the eBOSS weights file exceeds our newly trained weights file in completeness with similar or better purity. This is partially due to our use of this confidence threshold when determining classification for active learning, as we only pick spectra that are confused between classes when the constituent networks of the ensemble are very confident in their own classifications. It is likely that if we had used a lower threshold we would see our network outperforming the eBOSS one at that specific threshold, as we do with a threshold of 0.95.

## 4.2 Results on Unlabeled Data

In this section we produce a weights file using the entirety of our DESI labeled data set as a possible replacement for the current eBOSS trained weights. When we do this we do not split the assembled truth table, and use the entire 6698 spectra in the truth table as input training data for the weights file. For validation purposes we use the finalized weights file and use it to classify and estimate redshifts for the entirety of the DESI DR1 “Guadalupe” release, a dataset of approximately 3.6 million unique spectra. In this section we will refer to the old weights file as the “eBOSS weights” and the weights produced by this work as the “DESI weights”.

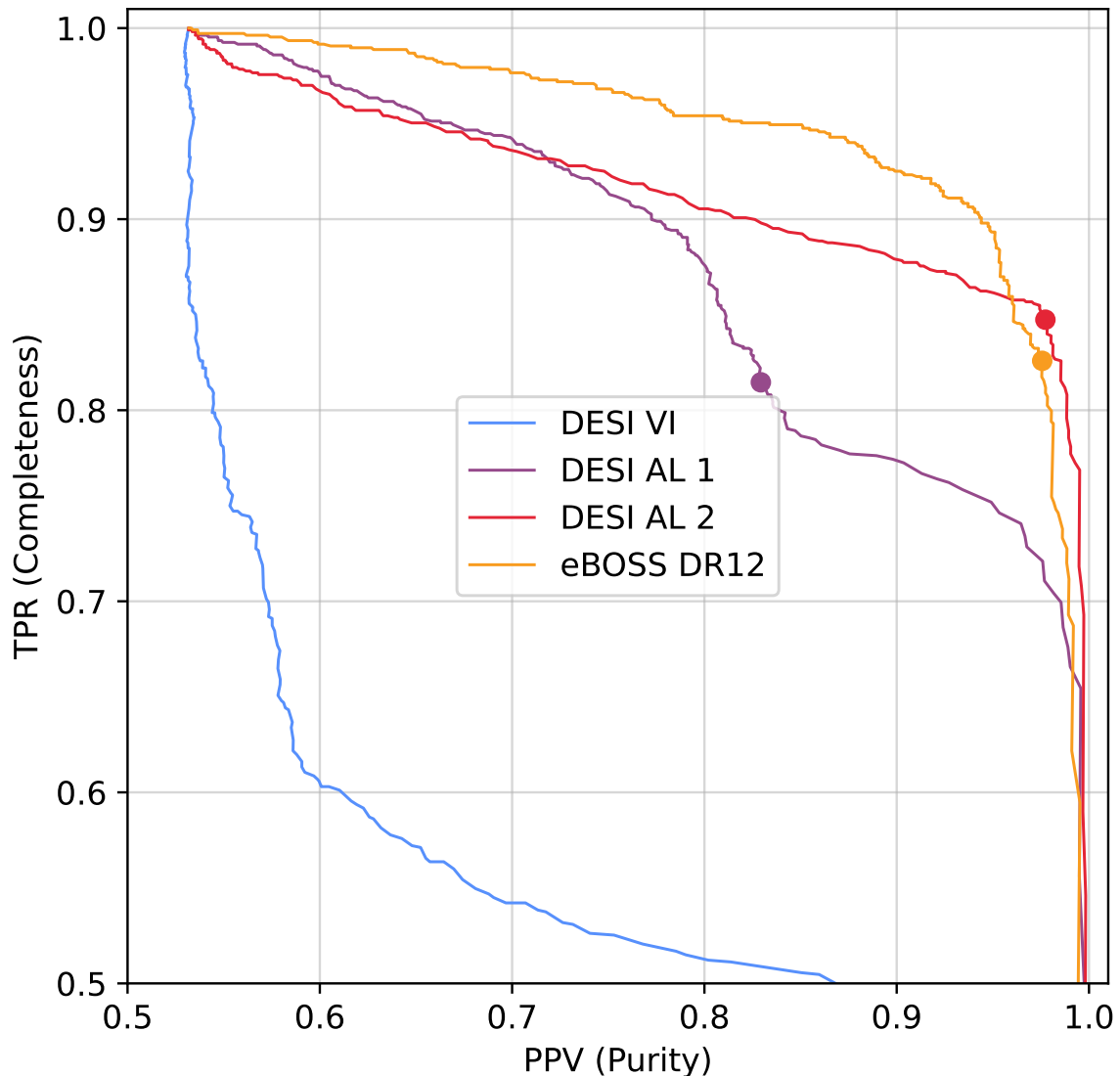


**Figure 6.** Plot of completeness versus purity for a variety of confidence thresholds ranging from zero to one. At each confidence threshold we compute quasar classifications and the corresponding completeness and purity on the validation dataset given those classifications. Colors match those of Fig. 4. A large dot on each curve (below the bottom of the plot for the original DESI visual inspection) denotes the values at the standard 0.95 confidence threshold. At a confidence threshold of 0.95, our new training post-active-learning outperforms the eBOSS weights file in completeness with a similar purity, although there are some threshold values at which the opposite is true.

#### 4.2.1 Classification and Consistency Results

In DESI Survey Validation we reobserved objects an average of 3 times. We can use these repeat observations to test the consistency of QuasarNET’s output from exposure to exposure. Each exposure will have its own noise and sky subtraction realizations, confounding the true signal in a unique way. Since the repeat exposures are of the same object, we quantify improvements as those by which the network more consistently classifies the object as the same class, whether that be a quasar or not, in exposures of the same object. Additionally

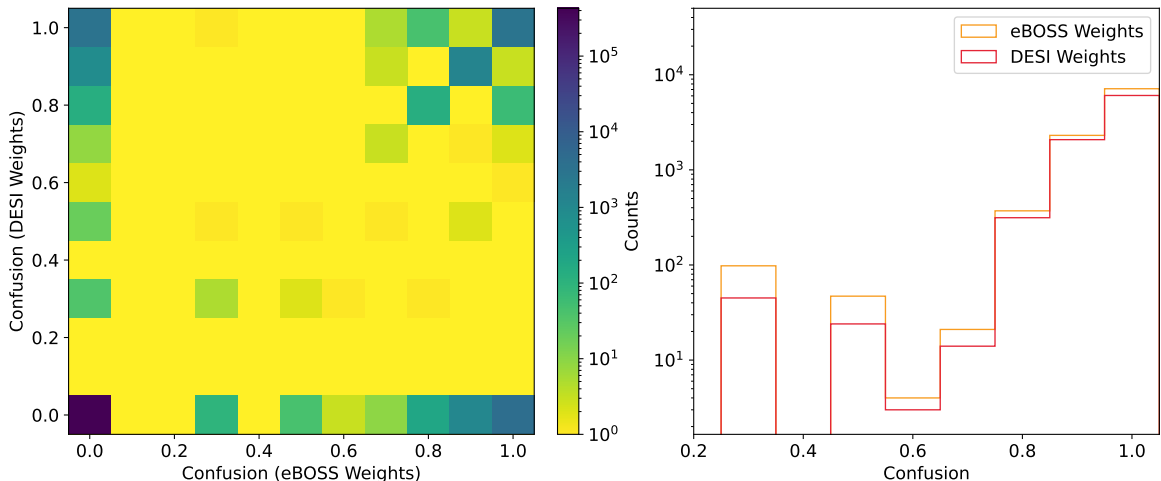


**Figure 7.** Confusion of repeat exposures of the same object from the eBOSS and DESI weights. See text for details on how we compute confusion. In the left panel is a two dimensional histogram, plotting the eBOSS confusion values vs the DESI confusion values. The bulk of the objects have no confusion, and thus a consistent classification across exposures. The right panel is a one dimensional histogram of confusion values, with the eBOSS results in blue and the DESI weights in orange. There is a notable decrease in all non-zero confusions values, with a corresponding increase in objects with zero confusion. For clarity we do not plot the zero confusion objects in the right histogram.

for those objects which QuasarNET does consistently classify as quasars we can compare the estimated redshift of each exposure to determine how secure the redshift estimation is from exposure to exposure.

In Figure 7 we plot the estimated confusion values for each weights file. For our purposes we use the entropy as defined in Eq. 3.2 to determine confusion, as it is symmetric, i.e. the entropy value when 60% of the exposures classified as a quasar and 40% are not is the same as 40% being quasars and 60% being not. Since in this case there are only two possible classifications the maximum confusion value is  $-\log_2 0.5 = 1$  when the classifications are equally split between being a quasar and not. A confusion of 0 is only achieved when QuasarNET produces the same classification on all exposures. The left panel is a two dimensional plot of confusion values, with the vertical axis being the confusion from the DESI weights and the horizontal axis being the confusion from the eBOSS weights, demonstrating where confusion values lie in this two dimensional space. The right panel overplots 1-D histograms of the two weights-files' results, underscoring the decrease in confusion values across all non-zero values with the new DESI weights. There is a corresponding slight increase in 0 values in the new DESI weights, but the overwhelming number of repeat exposures in that bin obfuscate this somewhat (note the logarithmic scaling on the vertical axis).

In Figure 8 we show the results of the redshift consistency test, plotting the standard deviation of redshift estimates of the same object versus the redshift. For clarity we create bins in redshift, represented in the plot by their mean redshift value, and take the mean of the standard deviation values in that bin. In blue are the eBOSS weight's redshift estimates, while below and in orange are the DESI weight's estimates. The DESI weights produce consistently lower variance in redshift estimates, representing an improvement in *consistency* of redshift estimates.

We would like to underscore that these results only validate that QuasarNET shows more

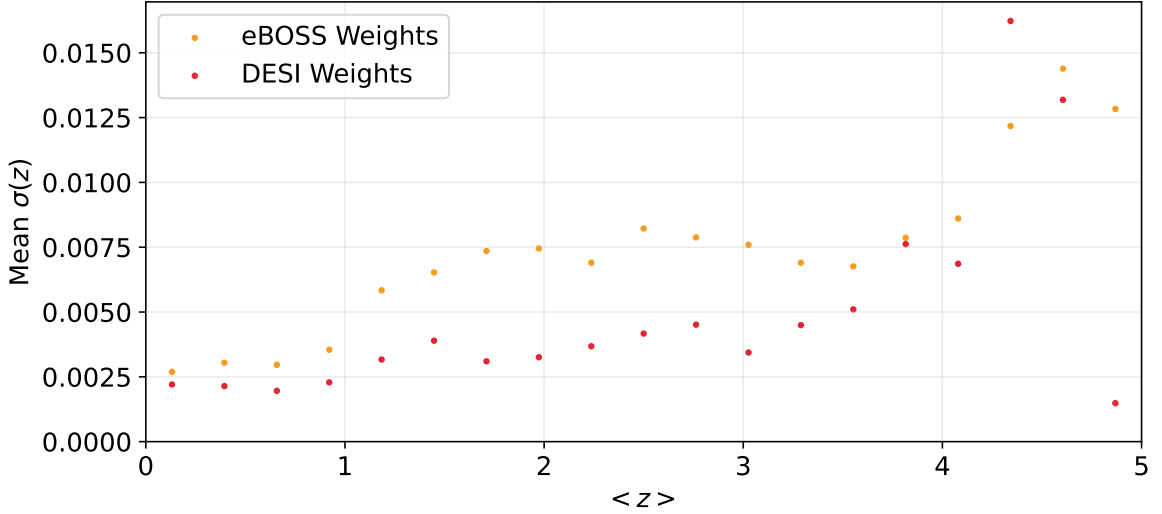


**Figure 8.** The mean binned standard deviation in redshift estimate. For each object we compute the standard deviation in redshift estimates from multiple exposures of the same object. Then we bin the objects in redshift, plotting the mean redshift of each bin and the mean of the standard deviations of the objects in that bin. In blue are the results from the prior eBOSS weights, and in orange are the results of the DESI weights. All bins above  $z = 4$  have low numbers of objects and corresponding higher variability. In all bins except one we produce more consistent redshift estimates.

consistency and less variability in results. This does not necessarily mean that QuasarNET is more accurate with the new weights file, just that it gets the same result more often. Indeed, when comparing the redshift estimates between the new and old weights files we discovered that both weights files share an issue with redshift estimation.

#### 4.2.2 Redshift Results and Identifying an Issue with QuasarNET

Using the aforementioned DESI DR1 supplement we computed redshift estimates for all spectra and compared them to the original classification and redshift estimates from the previous weights file. This comparison is shown in Figure 9. Plotted is a comparison of different redshift estimates between the eBOSS and DESI weights files. Only spectra for which both weights files classify the object as a quasar are included in the plot, as QuasarNET does not produce redshift estimates for non-quasar objects. The total number of spectra included in the plot is 273,319, accounting for about 7.52% of the total dataset.

The bulk of the redshift estimates lie close to the main diagonal. In order to quantify how many redshift estimates lie close to the diagonal and their level of agreement between the two weights files we compute the recession velocity of the quasar from both redshift estimates and compare. For recession velocity we use  $v(z) = \frac{D_c(z)}{1+z}H(z)$ , where  $D_c(z)$  is the comoving distance, using the fiducial cosmology favored in [15], which includes mild curvature, although the recession velocities are relatively robust to changes in cosmological parameters. Using these recession velocities, 89% of redshift estimates agree between the eBOSS and DESI weights within  $\Delta v \leq 3000\text{km/s}$ . 97.6% of the estimates agree within  $\Delta v \leq 5000\text{km/s}$ , indicating that an overwhelming number of redshift estimates agree within reason between the weights files. This is shown in the bottom panel of Figure 9, where we plot  $(z_{\text{DESI}} - z_{\text{eBOSS}})/(1 + z_{\text{eBOSS}}) = \Delta z/(1 + z_{\text{eBOSS}})$  along with two cutoff lines in

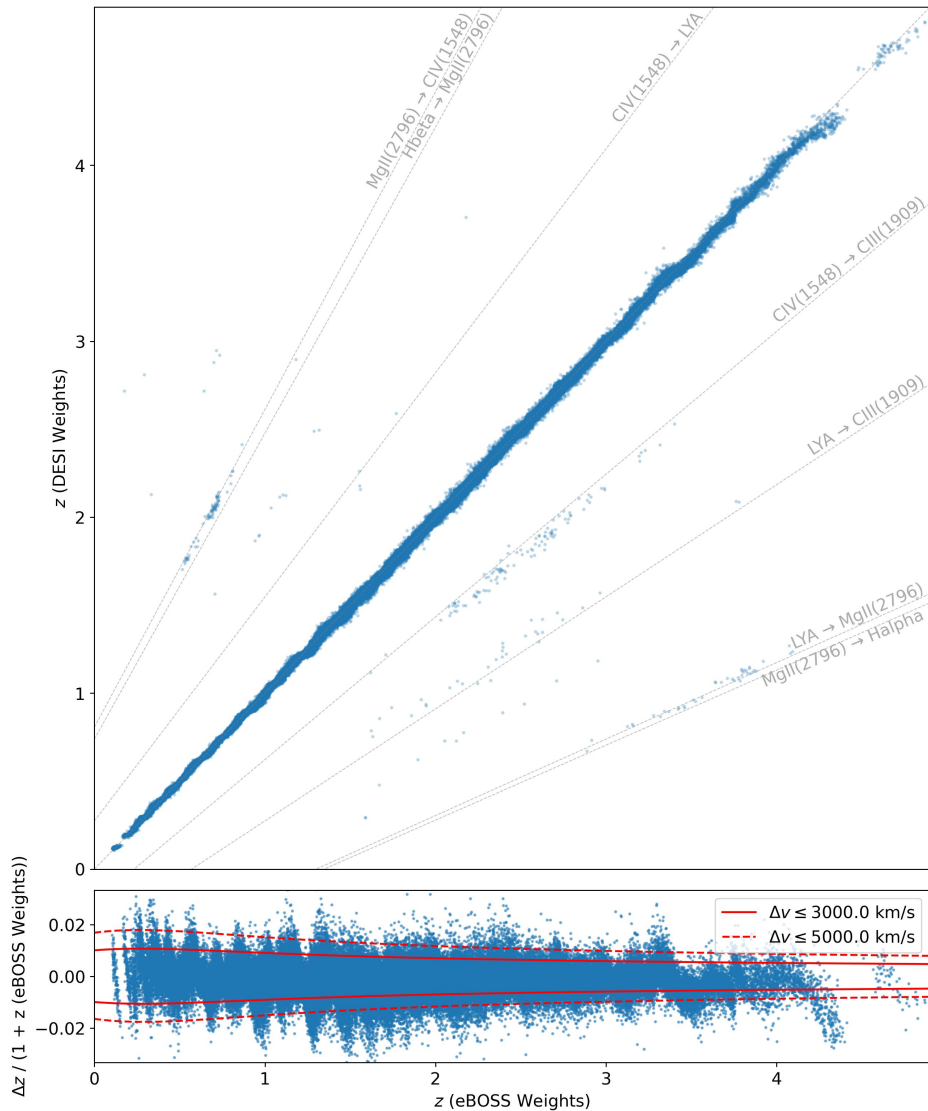


**Figure 9.** Comparison between redshift estimates from the prior (eBOSS) weights file and the new (DESI) weights file. The top panel is a square plot of the two redshift estimates, most redshift estimates lie close to or along the diagonal where  $z_{\text{eBOSS}} \approx z_{\text{DESI}}$ . Some redshift estimates lie off the diagonal, and can be linked to “line confusions” where both networks are using the same observed-frame emission line to estimate redshift but differ in which rest-frame emission line they use for redshift estimation. Some of these line confusions are plotted as diagonal dashed grey lines, with the corresponding label at the right most edge of the line where the first line is the rest-frame line used by the eBOSS weights file and the second line is the rest-frame line used by the DESI weights file. In the bottom panel we plot  $\Delta z / (1 + z_{\text{eBOSS}})$  to compare how significant the deviations from a perfect diagonal agreement are. The two cutoffs used in the text are plotted in dashed red ( $\Delta v \leq 3000$  km/s) and solid red ( $\Delta v \leq 5000$  km/s), with 89% and 97.6% of estimates falling within the respective curves. “Oscillations” around the diagonal are present in both panels, see text for an explanation.

dashed and solid red corresponding to the two aforementioned agreements respectively. The redshift estimation of the eBOSS weights file for DESI was validated previously in [22] and the significant agreement in redshift estimates reinforces that our new DESI weights file is

performing at a similar or better level of success to the previous weights file.

Some off-diagonal redshift changes can be explained by “line-confusion,” which is when two different weights files estimate redshift based on the position of the same emission line, but predict that the observer-frame emission line corresponds to two different emission lines in the rest-frame. This swap in line classification leads to an easily predictable change in redshift estimation. Some clearly identifiable line confusions are plotted along diagonals in light, dashed, gray along with associated labels. The first line name in each label is the predicted associated rest-frame line from the eBOSS weights, where the second is the prediction from the DESI weights.

In spectra that lie along the diagonal and have some measure of agreement in redshift estimates, we identify oscillations around perfect agreement. This can be seen prominently in the bottom panel where we plot the delta of the two redshift estimates. These oscillations correspond exactly with the edges of the QuasarNET output boxes used for line position estimation. Our active learning dataset, while correctly improving classification accuracy, had the unintended side effect of revealing a deficiency in QuasarNET’s redshift estimation. QuasarNET divides the output wavelength grid into 13 discrete boxes and has a tendency to clump line position estimates towards the center of the boxes. This effect can be obfuscated by including more data at all redshifts, correspondingly including more variety in line position and shape, which is why the effect is less prominent in the eBOSS weights compared to the DESI weights, even though it is still present. While this work did make this issue more prevalent, allowing us to discover and understand it, it is undesirable to keep in the final weights file for DESI processing. For DESI’s Year 3 processing we returned these oscillations to at or below the eBOSS level by including a larger set of training data comprised of DESI spectra with VI labels cross matched from eBOSS. This improved QuasarNET’s coverage at all redshifts, and mitigated the oscillations, but does not solve the underlying problem which is inherent in the construction of QuasarNET.

## 5 Conclusions

In this paper we have made significant changes to QuasarNET to improve its classification performance for use in the spectral processing pipeline for DESI. Since QuasarNET was originally designed and trained on eBOSS data, we chose to make modifications to QuasarNET that would improve its performance on DESI data. One of these changes included training on only labeled DESI data, a significantly reduced dataset compared to that of the previous eBOSS trained weights file.

In order to accommodate the reduced amount of training data we modified the structure of QuasarNET by including dropout layers and two additional convolution blocks. Both of these changes improve the generalizability of QuasarNET when trained on a reduced training set, an inherent problem when using DESI data only for training. Since visual inspection of DESI data has only been carried out on small subsamples of the full dataset, we only have approximately 4600 spectra available to use for training, a significant decrease compared to the eBOSS weights file.

After modifying QuasarNET directly we then increased the amount of training data available by doing two additional rounds of visual inspection. In order to optimally distribute our limited human effort and time we use an algorithm called active learning to select which data to visually inspect. In our active learning pipeline we use bootstrapping to generate 200 separate and unique networks from the same (minimal) training dataset. These networks

classify each spectrum into three categories, LOWZ, HIGHZ and NOT QSO. We then applied a novel outlier rejection step to further optimize over time and effort to ensure that we only label spectra that are representative of the bulk sample of quasars observed in the DESI survey. Our novel outlier rejection step removes approximately 10% of possible data for labeling. Ultimately we produced a truth table of 6700 spectra for training, two spectra of which we removed due to data processing error, and used these spectra to train a new candidate weights file for the DESI survey.

When used on DESI data the new weights file has marginally better completeness with a significant improvement in purity, reducing the number of false positive quasar identifications. When comparing different exposures of the same object our new weights file produces more consistent classifications, more often classifying objects the same way in different exposures of the same object. For objects that are consistently classified as a quasar our new weights file also has a significantly lower spread in redshift estimates.

However, for objects classified as a quasar in both the old and new weights files, we note that even though the majority of our redshift estimates agree with the eBOSS weights predictions our weights file revealed minor issues with QuasarNET’s redshift estimation. QuasarNET tends to clump its line position estimates, in turn leading to wiggles or oscillations in redshift estimates. In this paper we focused exclusively on selecting spectra that would improve QuasarNET’s classification accuracy, but as a result discovered that our resulting training sample does not cover the entire redshift range. Further work into both understanding and removing these redshift wiggles is currently underway. For DESI’s Year 3 processing we have used the understanding of this problem, gained in this paper, to mitigate these issues by including an additional set of DESI training data cross matched from eBOSS, thus returning the oscillations to the eBOSS levels while maintaining the improved classification accuracy gained from the Active Learning pipeline.

## Acknowledgments

The work of Dylan Green and David Kirkby was supported by the U.S. Department of Energy, Office of Science, Office of High Energy Physics, under Award No. DE-SC0009920.

This material is based upon work supported by the U.S. Department of Energy (DOE), Office of Science, Office of High-Energy Physics, under Contract No. DE-AC02-05CH11231, and by the National Energy Research Scientific Computing Center, a DOE Office of Science User Facility under the same contract. Additional support for DESI was provided by the U.S. National Science Foundation (NSF), Division of Astronomical Sciences under Contract No. AST-0950945 to the NSF’s National Optical-Infrared Astronomy Research Laboratory; the Science and Technology Facilities Council of the United Kingdom; the Gordon and Betty Moore Foundation; the Heising-Simons Foundation; the French Alternative Energies and Atomic Energy Commission (CEA); the National Council of Humanities, Science and Technology of Mexico (CONAHCYT); the Ministry of Science, Innovation and Universities of Spain (MICIU/AEI/10.13039/501100011033), and by the DESI Member Institutions: <https://www.desi.lbl.gov/collaborating-institutions>. Any opinions, findings, and conclusions or recommendations expressed in this material are those of the author(s) and do not necessarily reflect the views of the U. S. National Science Foundation, the U. S. Department of Energy, or any of the listed funding agencies.

The authors are honored to be permitted to conduct scientific research on Iolkam Du’ag (Kitt Peak), a mountain with particular significance to the Tohono O’odham Nation.

**Data Availability** All data and python code used to generate the plots in this paper are accessible at <https://doi.org/10.5281/zenodo.15328537>.

## References

- [1] M. Levi, C. Bebek, T. Beers, R. Blum, R. Cahn, D. Eisenstein et al., *The DESI Experiment, a whitepaper for Snowmass 2013*, *arXiv e-prints* (2013) arXiv:1308.0847 [[1308.0847](#)].
- [2] DESI Collaboration, A. Aghamousa, J. Aguilar, S. Ahlen, S. Alam, L.E. Allen et al., *The DESI Experiment Part I: Science, Targeting, and Survey Design*, *arXiv e-prints* (2016) arXiv:1611.00036 [[1611.00036](#)].
- [3] DESI Collaboration, A. Aghamousa, J. Aguilar, S. Ahlen, S. Alam, L.E. Allen et al., *The DESI Experiment Part II: Instrument Design*, *arXiv e-prints* (2016) arXiv:1611.00037 [[1611.00037](#)].
- [4] DESI Collaboration, B. Abareshi, J. Aguilar, S. Ahlen, S. Alam, D.M. Alexander et al., *Overview of the Instrumentation for the Dark Energy Spectroscopic Instrument*, *The Astronomical Journal* **164** (2022) 207 [[2205.10939](#)].
- [5] J.H. Silber, P. Fagrelus, K. Fanning, M. Schubnell, J.N. Aguilar, S. Ahlen et al., *The Robotic Multiobject Focal Plane System of the Dark Energy Spectroscopic Instrument (DESI)*, *The Astronomical Journal* **165** (2023) 9 [[2205.09014](#)].
- [6] T.N. Miller, P. Doel, G. Gutierrez, R. Besuner, D. Brooks, G. Gallo et al., *The Optical Corrector for the Dark Energy Spectroscopic Instrument*, *The Astronomical Journal* **168** (2024) 95 [[2306.06310](#)].
- [7] C. Poppett, L. Tyas, J. Aguilar, C. Bebek, D. Bramall, T. Claybaugh et al., *Overview of the Fiber System for the Dark Energy Spectroscopic Instrument*, *The Astronomical Journal* **168** (2024) 245.
- [8] DESI Collaboration, A.G. Adame, J. Aguilar, S. Ahlen, S. Alam, D.M. Alexander et al., *DESI 2024 II: Sample Definitions, Characteristics, and Two-point Clustering Statistics*, *arXiv e-prints* (2024) arXiv:2411.12020 [[2411.12020](#)].
- [9] DESI Collaboration, A.G. Adame, J. Aguilar, S. Ahlen, S. Alam, G. Aldering et al., *Validation of the Scientific Program for the Dark Energy Spectroscopic Instrument*, *The Astronomical Journal* **167** (2024) 62 [[2306.06307](#)].
- [10] DESI Collaboration, A.G. Adame, J. Aguilar, S. Ahlen, S. Alam, G. Aldering et al., *The Early Data Release of the Dark Energy Spectroscopic Instrument*, *The Astronomical Journal* **168** (2024) 58 [[2306.06308](#)].
- [11] DESI Collaboration, M. Abdul-Karim, A.G. Adame, D. Aguado, J. Aguilar, S. Ahlen et al., *Data Release 1 of the Dark Energy Spectroscopic Instrument*, *arXiv e-prints* (2025) arXiv:2503.14745 [[2503.14745](#)].
- [12] DESI Collaboration, A.G. Adame, J. Aguilar, S. Ahlen, S. Alam, D.M. Alexander et al., *DESI 2024 III: Baryon Acoustic Oscillations from Galaxies and Quasars*, *arXiv e-prints* (2024) arXiv:2404.03000 [[2404.03000](#)].
- [13] DESI Collaboration, A.G. Adame, J. Aguilar, S. Ahlen, S. Alam, D.M. Alexander et al., *DESI 2024 V: Full-Shape Galaxy Clustering from Galaxies and Quasars*, *arXiv e-prints* (2024) arXiv:2411.12021 [[2411.12021](#)].
- [14] DESI Collaboration, A.G. Adame, J. Aguilar, S. Ahlen, S. Alam, D.M. Alexander et al., *DESI 2024 IV: Baryon Acoustic Oscillations from the Lyman Alpha Forest*, *arXiv e-prints* (2024) arXiv:2404.03001 [[2404.03001](#)].

- [15] DESI Collaboration, A.G. Adame, J. Aguilar, S. Ahlen, S. Alam, D.M. Alexander et al., *DESI 2024 VI: Cosmological Constraints from the Measurements of Baryon Acoustic Oscillations*, *arXiv e-prints* (2024) arXiv:2404.03002 [2404.03002].
- [16] DESI Collaboration, A.G. Adame, J. Aguilar, S. Ahlen, S. Alam, D.M. Alexander et al., *DESI 2024 VII: Cosmological Constraints from the Full-Shape Modeling of Clustering Measurements*, *arXiv e-prints* (2024) arXiv:2411.12022 [2411.12022].
- [17] J. Guy, S. Bailey, A. Kremin, S. Alam, D.M. Alexander, C. Allende Prieto et al., *The Spectroscopic Data Processing Pipeline for the Dark Energy Spectroscopic Instrument*, *The Astronomical Journal* **165** (2023) 144 [2209.14482].
- [18] E.F. Schlafly, D. Kirkby, D.J. Schlegel, A.D. Myers, A. Raichoor, K. Dawson et al., *Survey Operations for the Dark Energy Spectroscopic Instrument*, *The Astronomical Journal* **166** (2023) 259 [2306.06309].
- [19] S. Bailey, *Redrock: Spectroscopic classification and redshift fitting for the dark energy spectroscopic instrument*, *In Prep.* (2025) .
- [20] E. Chaussidon, C. Yèche, N. Palanque-Delabrouille, D.M. Alexander, J. Yang, S. Ahlen et al., *Target Selection and Validation of DESI Quasars*, *The Astrophysical Journal* **944** (2023) 107.
- [21] N. Busca and C. Balland, *QuasarNET: Human-level spectral classification and redshifting with Deep Neural Networks*, arXiv:1808.09955 [astro-ph] (2018) .
- [22] J. Farr, A. Font-Ribera and A. Pontzen, *Optimal strategies for identifying quasars in DESI*, *Journal of Cosmology and Astroparticle Physics* **2020** (2020) 015.
- [23] I. Pâris, P. Petitjean, N.P. Ross, A.D. Myers, É. Aubourg, A. Streblyanska et al., *The Sloan Digital Sky Survey Quasar Catalog: Twelfth data release*, *Astronomy & Astrophysics* **597** (2017) A79 [1608.06483].
- [24] S.A. Smee, J.E. Gunn, A. Uomoto, N. Roe, D. Schlegel, C.M. Rockosi et al., *The Multi-object, Fiber-fed Spectrographs for the Sloan Digital Sky Survey and the Baryon Oscillation Spectroscopic Survey*, *The Astronomical Journal* **146** (2013) 32.
- [25] G.E. Hinton, N. Srivastava, A. Krizhevsky, I. Sutskever and R.R. Salakhutdinov, *Improving neural networks by preventing co-adaptation of feature detectors*, July, 2012. 10.48550/arXiv.1207.0580.
- [26] N. Srivastava, G. Hinton, A. Krizhevsky, I. Sutskever and R. Salakhutdinov, *Dropout: A Simple Way to Prevent Neural Networks from Overfitting*, *Journal of Machine Learning Research* **15** (2014) 1929.
- [27] D.M. Alexander, T.M. Davis, E. Chaussidon, V.A. Fawcett, A. X. Gonzalez-Morales, T.-W. Lan et al., *The DESI Survey Validation: Results from Visual Inspection of the Quasar Survey Spectra*, *The Astronomical Journal* **165** (2023) 124.
- [28] T.-W. Lan, R. Tojeiro, E. Armengaud, J.X. Prochaska, T.M. Davis, D.M. Alexander et al., *The DESI Survey Validation: Results from Visual Inspection of Bright Galaxies, Luminous Red Galaxies, and Emission-line Galaxies*, *The Astrophysical Journal* **943** (2023) 68.
- [29] B. Settles, *Active Learning*, Synthesis Lectures on Artificial Intelligence and Machine Learning, Springer International Publishing, Cham (2012).
- [30] M. Lochner and B.A. Bassett, *Astronomy: Personalised active anomaly detection in astronomical data*, *Astronomy and Computing* **36** (2021) 100481.
- [31] M. Walmsley, L. Smith, C. Lintott, Y. Gal, S. Bamford, H. Dickinson et al., *Galaxy Zoo: probabilistic morphology through Bayesian CNNs and active learning*, *Monthly Notices of the Royal Astronomical Society* **491** (2020) 1554.

- [32] T. Kohonen, *Self-organized formation of topologically correct feature maps*, *Biological Cybernetics* **43** (1982) 59.
- [33] J.E. Geach, *Unsupervised self-organized mapping: a versatile empirical tool for object selection, classification and redshift estimation in large surveys*, *Monthly Notices of the Royal Astronomical Society* **419** (2012) 2633.
- [34] A.H. Wright, H. Hildebrandt, J.L.v.d. Busch and C. Heymans, *Photometric redshift calibration with self-organising maps*, *Astronomy & Astrophysics* **637** (2020) A100.
- [35] B. Abolfathi, *SOMVIZ*, 2022.